

Helicity cascades in rotating turbulence

P.D. Mininni^{1,2} and A. Pouquet²

¹*Departamento de Física, Facultad de Ciencias Exactas y Naturales, Universidad de Buenos Aires, Ciudad Universitaria, 1428 Buenos Aires, Argentina.*

²*NCAR, P.O. Box 3000, Boulder, Colorado 80307-3000, U.S.A.*

(Dated: November 8, 2018)

The effect of helicity (velocity-vorticity correlations) is studied in direct numerical simulations of rotating turbulence down to Rossby numbers of 0.02. The results suggest that the presence of net helicity plays an important role in the dynamics of the flow. In particular, at small Rossby number, the energy cascades to large scales, as expected, but helicity then can dominate the cascade to small scales. A phenomenological interpretation in terms of a direct cascade of helicity slowed down by wave-eddy interactions leads to the prediction of new inertial indices for the small-scale energy and helicity spectra.

I. INTRODUCTION

Invariants of the equations of motion play an essential role in the behavior of turbulent flows. The well-known cascade of energy to the small scales in three dimensional hydrodynamic turbulence, associated with the energy invariant, has been studied at length since the celebrated paper of Kolmogorov [1]. Less well understood is the role played by the second quadratic (but non positive definite) invariant of the Euler equations, namely the helicity which embodies the global correlations between the velocity field \mathbf{u} and the vorticity $\boldsymbol{\omega} = \nabla \times \mathbf{u}$. Helicity itself plays no role in the Kolmogorov (K41) theory of turbulence [1]. Shortly after the discovery that helicity is a quadratic invariant of the three-dimensional Euler equation [2] (see also [3]), two scenarios were put forward for its dynamical behavior [4]: a dual cascade of energy and helicity towards smaller scales, and a pure helicity cascade with no cascade of energy. Studies of absolute equilibrium ensembles for isotropic helical turbulence [5] gave support to the former scenario, a result that was later confirmed by two-point closure models of turbulence [6] as well as by direct numerical simulations (DNS) [7, 8, 9, 10, 11].

In non-rotating helical hydrodynamic turbulence, both the helicity and the energy cascade towards smaller scales with constant fluxes. The assumption that the transfer rates are determined by the energy flux alone gives Kolmogorov scaling in the inertial range of both quantities, as is observed in the numerical simulations. As a result, the presence of helicity may globally arrest the energy transfer (when \mathbf{u} is strictly parallel to $\boldsymbol{\omega}$, the nonlinear term – expressed in terms of the Lamb vector $\mathbf{u} \times \boldsymbol{\omega}$ – is zero to within a pressure term), but the energy cascade scaling does not differ from that of non-helical turbulence.

In rotating turbulence, helicity is still an inviscid quadratic invariant. Perhaps because of the existence of dual direct cascades in non-rotating turbulence, not much attention has been paid in the literature to the scaling of net helicity in the rotating case. Helical-wave decompositions were introduced in [12, 13] (see also [14, 15]) and were found useful in the study of rotating turbu-

lence [16, 17]. Theoretical predictions for the helicity spectrum in the presence of strong rotation were also given in [18] in the framework of weak turbulence, under the assumption of a dual cascade. Recently, the effect of helicity in free-decaying rotating turbulence was studied in numerical simulations [19]. It was observed that both effects inhibit the energy transfer through different mechanisms: helicity diminishes nonlinear interactions globally, whereas rotation concentrates nonlinear interactions to resonant triads of inertial waves.

The lack of detailed studies of rotating helical flows is remarkable considering the relevance of helicity in certain atmospheric processes [20, 21, 22], such as rotating convective (supercell) thunderstorms the predictability of which may be enhanced because of the increased stability associated to the weakening of the nonlinear terms.

Recently, high resolution numerical simulations of rotating flows with non-helical forcing [23] showed that, while the velocity and vorticity in real space develop anisotropies and large-scale column-like structures as expected, the spatial distribution of helicity is more homogeneous and isotropic and tends to have a short correlation length. This observation motivates the present study. We present results from DNS of rotating turbulent flows with helical forcing. The results suggest that rotating helical flows behave in a different way than rotating non-helical flows. In particular, an inverse cascade of energy and a direct cascade of energy and helicity are discussed, the latter novel insofar as the transfer rate to small scales is dominated by the helicity flux.

II. NUMERICAL SIMULATIONS

We solve numerically the equations for an incompressible rotating fluid with constant mass density,

$$\frac{\partial \mathbf{u}}{\partial t} + \boldsymbol{\omega} \times \mathbf{u} + 2\boldsymbol{\Omega} \times \mathbf{u} = -\nabla \mathcal{P} + \nu \nabla^2 \mathbf{u} + \mathbf{F}, \quad (1)$$

and

$$\nabla \cdot \mathbf{u} = 0, \quad (2)$$

TABLE I: Parameters used in the simulations. k_F gives the range of forcing wavenumbers, ν is the kinematic viscosity and Ω the rotation rate; Re , Ro , and Ek are respectively the Reynolds, Rossby and Ekman numbers. Runs are performed on grids of 512^3 points in all cases and up to 40 turn-over times.

Run	k_F	ν	Ω	Re	Ro	Ek
A1	7–8	6.5×10^{-4}	0.06	1200	7.9	6.5×10^{-3}
A2	7–8	6.5×10^{-4}	0.3	1200	1.6	1×10^{-3}
A3	7–8	6.5×10^{-4}	7	1200	0.07	6×10^{-5}
A4	7–8	6.5×10^{-4}	14	1200	0.03	2.5×10^{-5}
B1	2–3	6×10^{-4}	0.08	5700	2.1	4×10^{-4}
B2	2–3	6×10^{-4}	3.5	5700	0.05	9×10^{-6}
B3	2–3	6×10^{-4}	8	5700	0.02	3.5×10^{-6}

where \mathbf{u} is the velocity field, $\boldsymbol{\omega} = \nabla \times \mathbf{u}$ is the vorticity, \mathcal{P} is the total pressure (modified by the centrifugal term) divided by the mass density, and ν is the kinematic viscosity. Here, \mathbf{F} is an external force that drives the turbulence, and we choose the rotation axis to be in the z direction: $\boldsymbol{\Omega} = \Omega \hat{z}$, with Ω the rotation frequency.

Eq. (1) is solved using a parallel pseudospectral code in a three dimensional box of size 2π with periodic boundary conditions and with a spatial resolution of 512^3 regularly spaced grid points. The pressure is obtained by taking the divergence of Eq. (1), using the incompressibility condition (2), and solving the resulting Poisson equation. The equations are evolved in time using a second order Runge-Kutta method, and the code uses the 2/3-rule for dealiasing. As a result, the maximum wavenumber is $k_{\max} = N/3$ where N is the number of grid points in each direction. The code is fully parallelized with the message passing interface (MPI) library [24, 25].

The mechanical forcing \mathbf{F} in Eq. (1) is given by the Arn'old-Beltrami-Childress (ABC) flow [26]

$$\mathbf{F} = F_0 \{ [B \cos(k_F y) + C \sin(k_F z)] \hat{x} + [C \cos(k_F z) + A \sin(k_F x)] \hat{y} + [A \cos(k_F x) + B \sin(k_F y)] \hat{z} \}, \quad (3)$$

where F_0 is the forcing amplitude, $A = 0.9$, $B = 1$, $C = 1.1$ [27], and k_F is the forcing wavenumber. The ABC flow is an eigenfunction of the curl with eigenvalue k_F ; as a result, when used as a forcing function, it injects both energy and helicity in the flow. Table I gives the parameters used in the simulations. All runs are well resolved and were continued for over 40 turnover times. Runs A1 and B1 were started from a fluid at rest, while the rest of the runs in sets A and B were started from the turbulent steady state reached at the end of runs A1 and B1 respectively.

The Reynolds, Rossby, and Ekman numbers are defined as usual as:

$$Re = \frac{L_F U}{\nu}, \quad (4)$$

$$Ro = \frac{U}{2\Omega L_F}, \quad (5)$$

and

$$Ek = \frac{Ro}{Re} = \frac{\nu}{2\Omega L_F^2}. \quad (6)$$

where $L_F = 2\pi/k_F$, and the turnover time at the forcing scale is then defined as $T = L_F/U$ where $U = \langle u^2 \rangle$ is the *r.m.s.* velocity measured in the turbulent steady state or when the inverse cascade of energy starts (see below). The dissipation wavenumbers k_η quoted below correspond to the Kolmogorov wavenumber $k_\eta = (\epsilon/\nu^3)^{1/4}$, where ϵ is the energy injection rate.

In the following, it will be useful to introduce a micro-Rossby number as the ratio of *r.m.s.* vorticity to the background vorticity (rotation),

$$Ro_\omega = \frac{\omega}{2\Omega}. \quad (7)$$

The value of the micro-Rossby number plays a central role in the inhibition of the energy cascade in rotating turbulence [16]. If the micro-Rossby number is too small, non-linear interactions are completely damped. According to [28], anisotropies develop in rotating flows when the Rossby number $Ro \lesssim 1$ and when the micro-Rossby number $Ro_\omega \gtrsim 1$ (it is worth noting that the actual values for the transition depend on the particular flow studied).

The energy integral scale is given by

$$L = 2\pi \frac{\int_1^{k_{\max}} E(k) k^{-1} dk}{\int_1^{k_{\max}} E(k) dk}, \quad (8)$$

where $E(k)$ is the isotropic energy spectrum (defined by averaging in Fourier space over spherical shells). An integral scale for the helicity can also be defined as

$$L^H = 2\pi \frac{\int_1^{k_{\max}} H(k) k^{-1} dk}{\int_1^{k_{\max}} H(k) dk}. \quad (9)$$

where $H(k)$ is the isotropic helicity spectrum. Perpendicular and parallel integral scales (e.g., L_\perp and L_\parallel) are useful to measure the development of anisotropies and are defined by replacing k by k_\perp or k_\parallel in Eqs. (8) and (9). Here, the wavenumbers k_\perp and k_\parallel denote the reduced spectra – e.g., $E(k_\perp)$ and $E(k_\parallel)$ – computed averaging in Fourier space respectively over cylinders and over planes (see [23] for more details).

III. NUMERICAL RESULTS

A. Energy inverse cascade at low Rossby numbers

For strong rotation, it is known that the flow becomes quasi two-dimensional and an inverse cascade of energy is expected [12, 13]. Figure 1 shows the energy and helicity

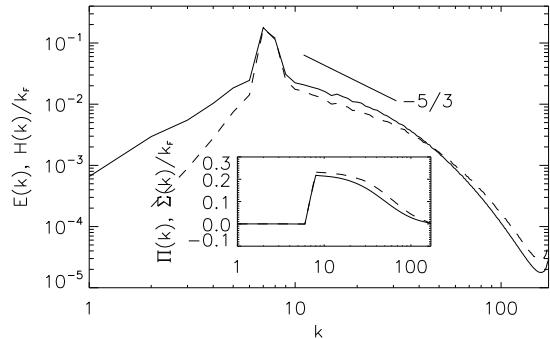


FIG. 1: Energy (solid line) and helicity (dash line) spectra in run A2 with forcing around $k \approx 7.5$ and almost negligible rotation. The inset shows the energy and helicity fluxes indicative of two classical direct cascades.

spectra at late times in run A2, for a moderate Rossby number, as well as their fluxes. One observes that the flux of energy $\Pi(k)$ and of helicity $\Sigma(k)$ are both negligible for $k < k_F$ and are of order unity and positive at wavenumbers larger than the forcing wavenumber k_F (here and in the following, the helicity spectrum and flux are plotted normalized by the forcing wavenumber k_F , to have them of the same order than the energy spectrum and flux when helicity injection is maximal). The inertial ranges of both the energy and helicity show similar scaling, close to K41 except for bottleneck (and possibly intermittency) corrections. Similar results are obtained in run A1 which has hardly any rotation effect.

However, runs A3 and A4 at low Rossby number show a different behavior (see Fig. 2): at scales larger than the forcing scale, an inverse cascade of energy is observed, with constant and negative energy flux, and with its amplitude roughly an order of magnitude larger than in the large Rossby number case. However, the spectrum of helicity in this inverse range is approximately flat, and the flux of helicity towards large scales is almost negligible.

The development of anisotropies and the inverse cascade of energy in rotating flows, leading for example to zonal flows in planetary atmospheres, has been explained in terms of near-resonant triad interactions of inertial waves: energy in three dimensional modes is transferred by a subset of the resonant interactions to modes with smaller vertical wavenumber [12, 13], a process that drives the flow to be quasi-two dimensional at large scales. The lack of an inverse transfer of helicity to large scales can be understood considering the partial two-dimensionalization of the flow at large scales: a helical flow is three-dimensional, while a two-dimensional flow has no helicity. Indeed, the energy spectra and fluxes in the direction perpendicular to Ω are similar to the isotropic spectrum (see Fig. 3), while the spectrum in the direction parallel to Ω peaks at $k_{\parallel} = 0$ (details of how much energy is in the modes with $k_{\parallel} = 0$ in each run are given in Table II).

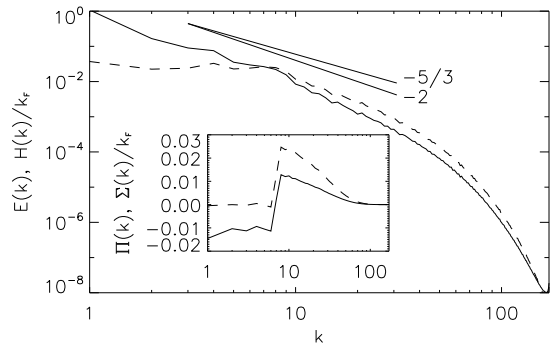


FIG. 2: Energy (solid) and helicity (dash) spectra in run A3 with same forcing than run A2 but lower Rossby number. Different slopes are shown as a reference. The inset gives the energy and helicity fluxes and shows that there is both a direct and an inverse cascade of energy but only a direct cascade of helicity.

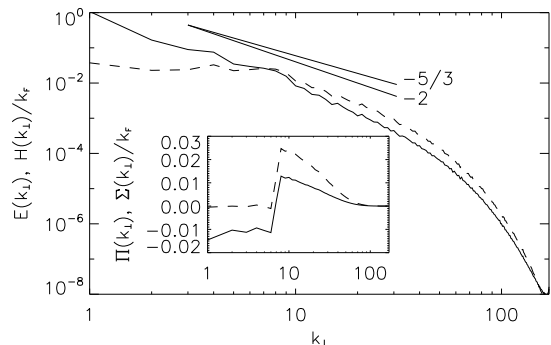


FIG. 3: Energy (solid) and helicity (dash) spectra as a function of k_{\perp} in run A3. Different slopes are shown as a reference. The inset shows the energy and helicity fluxes in terms of k_{\perp} .

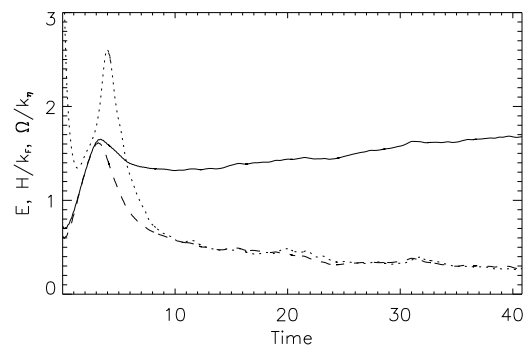


FIG. 4: Time evolution of the energy (solid), helicity (dash), and enstrophy (dot) in run A3. The helicity is normalized by k_F , and the enstrophy is rescaled by the dissipation wavenumber $k_{\eta} \approx 100$. Only the energy undergoes an inverse cascade, thereby growing with time.

TABLE II: Anisotropies measured at $t \approx 40$ in all runs. Ro_ω is the micro-Rossby number as defined in Eq. (7), L_\perp/L_\parallel is the ratio of perpendicular to parallel integral scales as defined in Eq. (8), L_\perp^H/L_\parallel^H is the same ratio but based on the helicity spectrum as in Eq. (9), $E(k_\parallel = 0)/E$ is the ratio of energy in all modes with $k_\parallel = 0$ to the total energy, and $H(k_\parallel = 0)/H$ is the ratio of helicity in those modes to the total helicity.

Run	Ro_ω	L_\perp/L_\parallel	L_\perp^H/L_\parallel^H	$E(k_\parallel = 0)/E$	$H(k_\parallel = 0)/H$
A1	160	0.56	0.56	0.05	0.04
A2	31	0.55	0.55	0.06	0.05
A3	0.6	1.28	0.53	0.95	0.74
A4	0.2	1.27	0.49	0.98	0.90
B1	95	0.86	0.85	0.30	0.33
B2	1.1	1.51	1.20	0.96	0.85
B3	0.5	1.36	1.07	0.96	0.86

The absence of an inverse cascade of helicity is further confirmed by the time evolution of the total energy, helicity and enstrophy (see Fig. 4). While the energy increases monotonically after $t \approx 10$, the helicity and the enstrophy decay until reaching a steady state after $t \approx 25$. The monotonic increase of the total energy is the result of the piling up of energy at $k_\perp = 1$ as the inverse cascade develops over time.

However, the distributions of both the energy and the helicity become anisotropic as time evolves. Table II gives the micro-Rossby number for all the runs at $t \approx 40$, the ratios of perpendicular to parallel integral scales for the energy and for the helicity, L_\perp/L_\parallel and L_\perp^H/L_\parallel^H , and finally the amount of energy and helicity in the modes with $k_\parallel = 0$ normalized respectively by the total energy and helicity. As the Rossby number decreases, the ratios L_\perp/L_\parallel and L_\perp^H/L_\parallel^H increase. However, the ratio of scales based on the helicity is smaller than the ratio of scales based on the energy, specially in the runs in set A where there is a larger separation between the largest scale in the box and the injection scale. This trend is accompanied by an increase in the amount of energy and helicity in the modes with $k_\parallel = 0$, although here again the ratio $E(k_\parallel = 0)/E$ is larger than $H(k_\parallel = 0)/H$. This can be understood in terms of the Schwarz inequality for each mode in Fourier space. As the energy undergoes an inverse cascade, some helicity is transferred to the large scales (note the flat spectrum of helicity at large scales in Fig. 2 compared with the steep spectrum in Fig. 1). According to the instability assumption of [13] (see also [29] and [12]), the energy is transferred toward modes with wavevectors perpendicular to the rotation axis. From the Schwarz inequality, the helicity in each wave mode \mathbf{k} must satisfy $|H(\mathbf{k})| \leq |\mathbf{k}|E(\mathbf{k})$, and the large scale helicity must be transferred towards k_\perp to satisfy this relation.

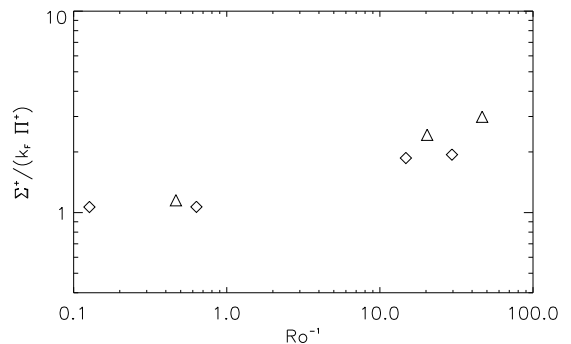


FIG. 5: Ratio of helicity flux to energy flux towards small scales as a function of inverse Rossby number and at a fixed Reynolds number for each set (see Table I). Diamonds correspond to runs in set A, and triangles correspond to runs in set B. Note the increase in relative strength of the helicity cascade to small scales as rotation increases.

B. The case for direct cascades

At scales smaller than the forcing scale, the energy spectrum in runs A3 and A4 at low Rossby numbers is slightly steeper than k^{-2} (see Fig. 3), and (unlike the case of non-rotating turbulence), the helicity spectrum is possibly shallower than the energy spectrum (a confirmation of this using runs in set B is discussed below). Furthermore (see Fig. 5), the energy flux $\Pi(k)$ becomes smaller than the (normalized) helicity flux $\Sigma(k)/k_F$ at wavenumbers larger than k_F as the Rossby number is decreased.

This change can be understood as follows. The energy injection rate ϵ and the helicity injection rate δ are related by $\delta \sim k_F \epsilon$ (these two quantities are equal when maximally helical forcing is applied at a single wavenumber). The Schwarz inequality in each shell $|H(k)| \leq kE(k)$ implies that, at large scale (in the limit $k \rightarrow 0$), there must be a negligible flux of helicity (unless of course $E(k) \rightarrow \infty$); thus helicity is bound to cascade to small scales. However, the development of an inverse cascade of energy decreases the amount of energy flux that can go to small scales, and as a result the helicity flux dominates for $k > k_F$. This can be illustrated by plotting the ratio $\Sigma^+/(k_F \Pi^+)$ (Fig. 5), where Σ^+ and Π^+ denote respectively the amount of helicity and energy flux that goes towards small scales. Note that $\Sigma^+/(k_F \Pi^+) \approx 1$ for $Ro > 1$ (both quantities direct cascade), while as the Rossby number decreases $\Sigma^+/k_F > \Pi^+$.

We can also introduce the differences between the direct and inverse energy and helicity fluxes, respectively as $\Delta\Sigma = (\Sigma^+ - \Sigma^-)/k_F$ and $\Delta\Pi = \Pi^+ - \Pi^-$ (where Σ^- and Π^- are negative and denote respectively the amount of helicity and energy that go towards large scales). Figure 6 shows the normalized ratio

$$\rho = (\Delta\Sigma + \Delta\Pi) / \Delta\Sigma .$$

This ratio is roughly independent of the Rossby number, which further confirms that the dominance of the helicity flux for $k > k_F$ is associated with the energy flux lost in that range because of the inverse cascade of energy.

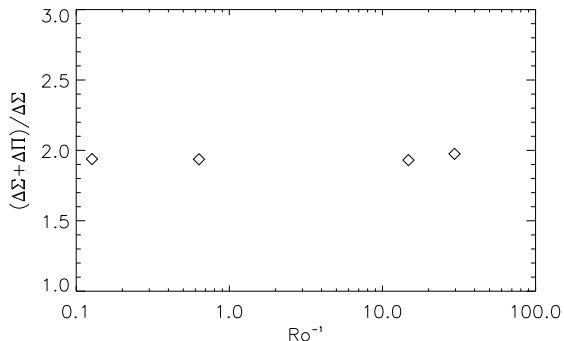


FIG. 6: Sum, for the energy and helicity, of the normalized differences between their direct and inverse fluxes (see text). Only runs in set A (diamonds) are shown because runs in set B do not have enough scale separation between the forcing and the largest scale in the box to compute Σ^- and Π^- reliably.

As a result, the direct transfer in the small scales of a rotating helical turbulent flow is dominated by the (normalized) helicity flux. In the limit of a pure helicity cascade with no direct energy cascade, and considering the effect of rotation, the helicity flux can be expressed as

$$\Sigma(k) \sim \delta \sim \frac{h_\ell}{\tau_\ell^2} \tau_\Omega, \quad (10)$$

where h_ℓ is the helicity at the scale ℓ , $\tau_\ell \sim \ell/u_\ell$ is the eddy turnover time at the same scale, and $\tau_\Omega \sim 1/\Omega$ is the characteristic time of inertial waves. This expression takes into account the slowing-down of transfer to small scales due to three-wave interactions (see e.g., [30, 31]), in a similar fashion as what was proposed by Iroshnikov and Kraichnan for Alfvén waves in the presence of a magnetic field [32, 33] (the extension to the anisotropic case can be trivially obtained considering the turnover time as $\tau_\ell \sim \ell_\perp/u_\ell$, see e.g., [31]). From this expression, it follows that if $E(k) \sim k^{-n}$ ($n \leq 2.5$, with the equality holding for the case with maximum helicity at all scales from Schwarz inequality), then

$$H(k) \sim k^{n-4}, \quad (11)$$

i.e., resulting in a shallower helicity spectrum for $n \geq 2$ (note that for $n < 2$ the helicity spectrum is steeper than the energy spectrum).

Although the runs in set A have a helicity spectrum that is indeed slightly shallower than the energy spectrum, the forcing is applied at intermediate scales and the scale separation between the forcing and dissipative scales is not enough to confirm the scaling prediction of Eq. (11). Indeed, the micro-Rossby numbers are

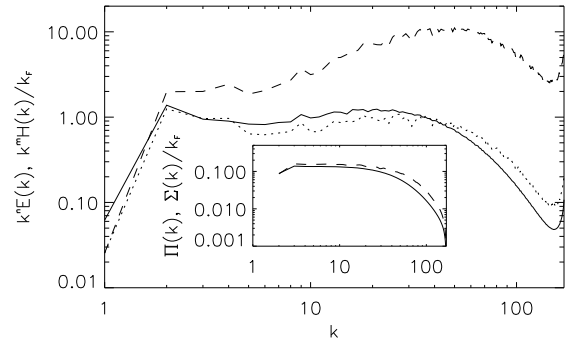


FIG. 7: Energy spectrum compensated by k^n with $n = 5/3$ (solid), helicity spectrum compensated by k^m with $m = n$ (dots), and compensated by $m = n - 4 \approx 2.33$ (dash line), in run B1 with large-scale forcing and weak rotation. Note that the helicity and the energy in this run have the same Kolmogorov scaling in the inertial range. The inset shows the energy and normalized helicity fluxes with solid and dash lines respectively.

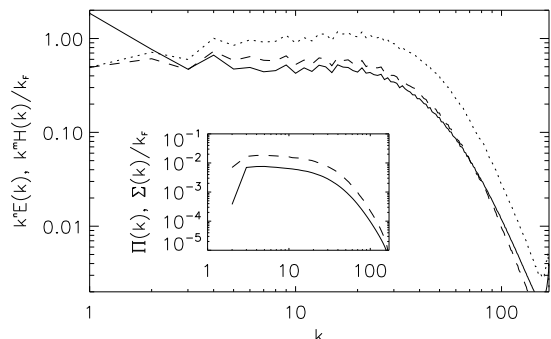


FIG. 8: Energy spectrum compensated by k^n with $n = 2.15$ (solid), helicity spectrum compensated by k^m with $m = n$ (dot), and compensated by $m = n - 4 = 1.85$ (dash line), in run B2 with large-scale forcing and low Rossby number. Note that the helicity and the energy spectra in this run have different scalings in the inertial range (different from each other and different from K41), and both are flat only when compensated following Eq. (11). The inset again shows the energy and (normalized) helicity fluxes; note the domination of the latter in this high-rotation regime.

$Ro_\omega \approx 0.6$ for run A3 and ≈ 0.2 for run A4 (see Table II). A larger direct inertial range and larger micro-Rossby numbers are needed in order to check the validity of the predicted scaling.

To that effect, we now report on the runs in set B (see Tables I and II) which have a forcing function concentrated in the large scales; the inverse cascade is thus not so well resolved but it allows for a more developed direct inertial range. In particular, we will focus on run B2 which as a Rossby number $Ro \approx 0.05$ and a micro-Rossby number $Ro_\omega \approx 1.1$. Figures 7 and 8 show the

compensated energy and helicity spectra for runs B1 and B2 (run B3 behaves as run A3). It is observed that while in run B1 (corresponding to weak rotation), the helicity and energy spectra have the same scaling ($\sim k^{-5/3}$ with bottleneck and intermittency corrections), in run B2 the compensated helicity and energy spectra are horizontal and parallel only when using the scaling law predicted by Eq. (11).

The same scaling is observed in k_{\perp} . As previously mentioned, it is straightforward to recast Eqs. (10) and (11) to take into account the anisotropies in the flow, again similarly to the magnetohydrodynamic case. The results exemplified by Fig. 8 confirm that the small-scale scaling of energy and helicity differ in rotating turbulence, unlike the non-rotating case (see e.g., Fig. 7) where energy and helicity follow the same spectral laws.

IV. CONCLUSION

Even though the Rossby number in the atmosphere of the Earth is not very large, the existence of inertial waves that can interact with turbulent eddies is bound to affect the dynamics of the turbulent flow, as has been studied by several authors. Helicity, which is also observed in atmospheric flows, is known to play an important role in the evolution of tornadoes. But, as already found in [19], the two physical phenomena (rotation on the one hand, helicity on the other hand) reduce nonlinear interactions in different ways. Thus a study combining both effects at high Reynolds number can shed some light on the dynamics of such flows.

This paper shows that for strong rotation, the direct cascade to small scales is now dominated by the helicity flux (and the inverse cascade, as expected, by the energy). Moreover, the resulting spectrum is different from what Kolmogorov scaling predicts for the non-rotating case, and from what a pure direct cascade of energy slowed down by eddy-wave interactions predicts for the rotating non-helical case. In this context it is worth mentioning that, using phenomenological arguments, a direct cascade

of helicity in rotating flows has also been argued recently in [34], although the arguments predicted a different scaling and were based on Fjortoft's theorem which does not necessarily apply to the helicity since it is not a positive definite quantity [5].

A novel phenomenological argument based on a cascade of helicity towards small scales slowed down by wave-eddy interactions lead to different inertial indices for the small-scale energy and helicity spectra, and provides a good fit to the results of the simulations presented in this paper. The spectral indices are bounded by the value that corresponds to a flow with maximum helicity, and depend on the amount of relative helicity in the flow. The result differs from non-rotating turbulence, where the energy and the helicity follow the same scaling laws [4, 8, 10]. Although the DNS runs confirm the scaling, due to computational limitations well-resolved inverse and direct cascades had to be studied in separate simulations. In the future, a simulation of helical rotating turbulence at very large resolution will be performed to confirm these results with a better resolved coexistence of the direct and inverse cascades.

The study of the intermittency of a mixture of turbulence and waves in the presence of rotation and helicity will also be the topic of a future work; it is of particular interest since it will shed some light on the statistics, structures and interactions of extreme events which, when combined with realistic physics of the atmosphere (e.g., adding weak compressibility, moisture and geometry), will lead eventually to a better understanding and prediction of the behavior of atmospheric flows.

Acknowledgments

Computer time was provided by NCAR. NCAR is sponsored by the National Science Foundation. PDM acknowledges support from grant UBACYT X468/08 and is a member of the Carrera del Investigador Científico of CONICET.

-
- [1] A. N. Kolmogorov, Dokl. Akad. Nauk SSSR **30**, 9 (1941).
 - [2] H. K. Moffatt, J. Fluid Mech. **35**, 117 (1969).
 - [3] R. Betchov, Phys. Fluids **4**, 925 (1961).
 - [4] A. Brissaud, U. Frisch, J. Léorat, M. Lesieur, and A. Mazure, Phys. Fluids **16**, 1366 (1973).
 - [5] R. H. Kraichnan, J. Fluid Mech. **59**, 745 (1973).
 - [6] J. C. André and M. Lesieur, J. Fluid Mech. **81**, 187 (1997).
 - [7] V. Borue and S. A. Orszag, Phys. Rev. E **55**, 7005 (1997).
 - [8] Q. Chen, S. Chen, and G. L. Eyink, Phys. Fluids **15**, 361 (2003).
 - [9] Q. Chen, S. Chen, G. L. Eyink, and D. D. Holm, Phys. Rev. Lett. **90**, 214503 (2003).
 - [10] D. O. Gómez and P. D. Mininni, Physica A **342**, 69 (2004).
 - [11] P. D. Mininni, A. Alexakis, and A. Pouquet, Phys. Rev. E **74**, 016303 (2006).
 - [12] C. Cambon and L. Jacquin, J. Fluid Mech. **202**, 295 (1989).
 - [13] F. Waleffe, Phys. Fluids A **5**, 677 (1993).
 - [14] A. Craya, *Contribution à l'analyse de la turbulence associée à des vitesses moyennes*, P.S.T. Ministère de l'Air, France, vol. 345 (1958).
 - [15] J. Herring, Phys. Fluids **17**, 859 (1974).
 - [16] C. Cambon, N. N. Mansour, and F. S. Godeferd, J. Fluid Mech. **337**, 303 (1997).
 - [17] L. M. Smith and F. Waleffe, Phys. Fluids **11**, 1608 (1999).
 - [18] S. Galtier, Phys. Rev. E **68**, 015301 (2003).

- [19] Y. Morinishi, K. Nakabayashi, and S. Ren, Japan Soc. Mech. Eng. Series B **44**, 410 (2001).
- [20] D. K. Lilly, J. Atmosph. Sc. **43**, 126 (1988).
- [21] B. W. Kerr and G. L. Darkow, Weath. and Forecast. **11**, 489 (1996).
- [22] P. M. Markowski, J. M. Straka, E. N. Rasmussen, and D. O. Blanchard, Mont. Weath. Rev. **126**, 2959 (1998).
- [23] P. D. Mininni, A. Alexakis, and A. Pouquet (2008), arXiv:0802.3714.
- [24] D. O. Gómez, P. D. Mininni, and P. Dmitruk, Adv. Sp. Res. **35**, 899 (2005).
- [25] D. O. Gómez, P. D. Mininni, and P. Dmitruk, Phys. Scripta **T116**, 123 (2005).
- [26] S. Childress and A. D. Gilbert, *Stretch, twist, fold: the fast dynamo* (Springer-Verlag, Berlin, 1995).
- [27] V. Archontis, S. B. F. Dorch, and A. Nordlund, Astron. Astrophys. **410**, 759 (2003).
- [28] L. Jacquin, O. Leuchter, C. Cambon, and J. Mathieu, J. Fluid Mech. **220**, 1 (1990).
- [29] H. P. Greenspan, J. Fluid Mech. **36**, 257 (1969).
- [30] Y. Zhou, Phys. Fluids **7**, 2092 (1995).
- [31] W.-C. Müller and M. Thiele, Europhys. Lett. **77**, 34003 (2007).
- [32] P. S. Iroshnikov, Sov. Astron. **7**, 566 (1963).
- [33] R. H. Kraichnan, Phys. Fluids **8**, 1385 (1965).
- [34] S. Chakraborty, Europhys. Lett. **79**, 14002 (2007).